



# Mercaptopropane-assisted synthesis of graphitic carbon-supported Pt nanoparticles for enhancing fuel cell start-stop performance

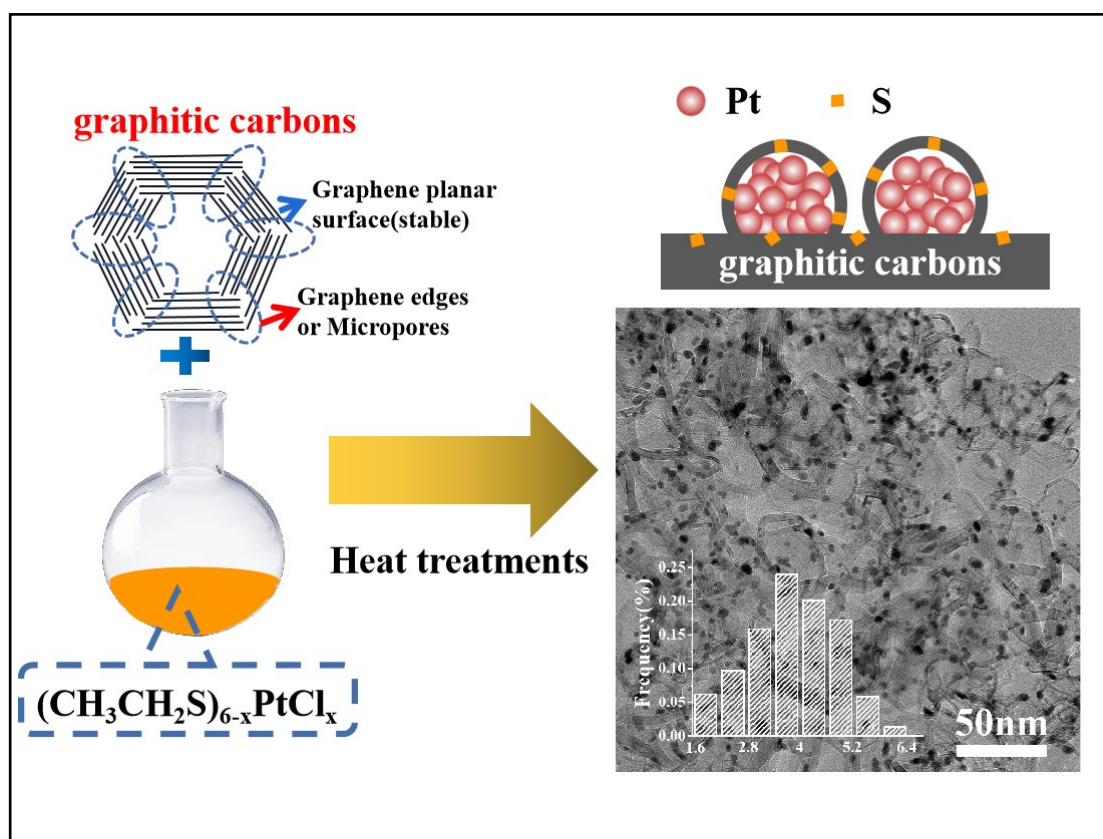
Qian-Qian Yang, Tian-Wei Song, Shuai Li, Le Zhang, Xiu-Yuan Ma, Lei Tong , and Hai-Wei Liang 

Hefei National Research Center for Physical Sciences at the Microscale, and Department of Chemistry, University of Science and Technology of China, Hefei 230026, China

Correspondence: Lei Tong, E-mail: [ltong17@mail.ustc.edu.cn](mailto:ltong17@mail.ustc.edu.cn); Hai-Wei Liang, E-mail: [hwliang@ustc.edu.cn](mailto:hwliang@ustc.edu.cn)

© 2023 The Author(s). This is an open access article under the CC BY-NC-ND 4.0 license (<http://creativecommons.org/licenses/by-nc-nd/4.0/>).

## Graphical abstract





*Mercaptopropane-assisted synthesis of graphitic carbon supported small-sized Pt nanoparticles.*

## Public summary

- A scalable and simple mercaptopropane-assisted impregnation method was developed for the preparation of small Pt nanoparticles on graphitic carbons.
- The resulting graphitic carbon-supported Pt nanoparticle catalysts demonstrated high durability under start-stop fuel cell operation.

# Mercaptopropane-assisted synthesis of graphitic carbon-supported Pt nanoparticles for enhancing fuel cell start-stop performance

Qian-Qian Yang, Tian-Wei Song, Shuai Li, Le Zhang, Xiu-Yuan Ma, Lei Tong , and Hai-Wei Liang 

Hefei National Research Center for Physical Sciences at the Microscale, and Department of Chemistry, University of Science and Technology of China, Hefei 230026, China

 Correspondence: Lei Tong, E-mail: [ltong17@mail.ustc.edu.cn](mailto:ltong17@mail.ustc.edu.cn); Hai-Wei Liang, E-mail: [hwliang@ustc.edu.cn](mailto:hwliang@ustc.edu.cn)

© 2023 The Author(s). This is an open access article under the CC BY-NC-ND 4.0 license (<http://creativecommons.org/licenses/by-nc-nd/4.0/>).



Cite This: *JUSTC*, 2023, 53(6): 0603 (8pp)



Read Online

**Abstract:** Although graphitic carbons, as a support for the cathode catalyst in proton exchange membrane fuel cells, have significant advantages in enhancing the corrosion resistance of the catalyst, the preparation of small-sized Pt particles on the graphitic carbon support often faces challenges due to its low porosity and lack of defect structures. Here, we report a mercaptopropane-assisted impregnation method to achieve size control of Pt nanoparticles on graphitic carbon. We show that mercaptopropane can coordinate with Pt during the impregnation process and transform into sulfur-doped carbon coatings through the subsequent thermal reduction process, which ensures the formation of small-sized Pt nanoparticles on graphitic carbon. Due to effective size control, the prepared cathode catalyst exhibited enhanced fuel cell performance compared to the catalyst prepared by the traditional impregnation method. We performed the accelerated stress test on the synthesized catalyst using the durability protocol recommended by the U.S. Department of Energy (DOE). After 5000 voltage cycles in the range of 1.0–1.5 V, the catalyst showed a negligible voltage loss of only 10 mV at a current density of 1.5 A·cm<sup>-2</sup>, meeting the DOE support durability target (30 mV).

**Keywords:** PEMFC; catalyst support durability; graphitic carbon; Pt; start-stop performance

**CLC number:** TQ426; TM911.4

**Document code:** A

## 1 Introduction

Polymer electrolyte membrane fuel cells (PEMFCs) represent a clean energy technology that holds promise for deployment in low-carbon transportation<sup>[1]</sup>. Reducing the amount of Pt used in the cathode without sacrificing performance and durability is crucial for achieving widespread commercialization of PEMFCs<sup>[2,3]</sup>. One fundamental consensus in this endeavor is the need to control the particle size of Pt to attain a balance between activity and durability in catalyzing the oxygen reduction reaction (ORR)<sup>[4,5]</sup>. Smaller Pt particles result in a larger electrochemically active surface area (ECSA), which enhances the mass activity (MA) of Pt<sup>[6–9]</sup>. However, particles that are too small can also cause a high electrochemical dissolution rate of Pt and poor durability, especially in the case of Pt nanoparticles with a diameter of < 2 nm<sup>[10]</sup>. In addition, achieving a uniform particle size distribution is beneficial to mitigate the dissolution rate of Pt because it can narrow differences in surface energy between particles<sup>[3,10,11]</sup>. In this regard, cathode catalysts are typically designed as carbon-supported Pt nanoparticle morphologies, where the carbon supports feature high specific surface areas that facilitate the preparation of Pt nanoparticles with relatively small sizes and uniform distribution<sup>[12]</sup>.

However, high surface area carbon supports are vulnerable to electrochemical corrosion, especially during the start-stop

operation: a hydrogen–oxygen interface can form during this operation in the anode region, which raises the cell voltage and accelerates carbon corrosion<sup>[13–16]</sup>. Severe carbon corrosion can result in a significant thinning of the cathode catalyst layer, accompanied by a considerable increase in oxygen transport resistance and detachment of abundant Pt nanoparticles from the support, ultimately leading to a substantial loss of performance<sup>[17–19]</sup>. While system operating strategies such as constraining the voltage range during operation can mitigate carbon corrosion, they impose additional costs for valves and controls<sup>[20–24]</sup>. As such, finding alternative support materials is deemed the fundamental solution to address the carbon-corrosion issue. There are currently two material-based solutions that have been thoroughly demonstrated to address this issue: the use of conductive metal oxides (such as TiO<sub>2</sub> and SnO<sub>2</sub>) and highly graphitized carbon materials as supports<sup>[25–27]</sup>. However, both of these solutions normally come with the trade-off of compromised performance<sup>[28,29]</sup>. This is mainly because both metal oxides and highly graphitized carbons have relatively low surface areas, which makes it difficult to achieve effective size control and dispersion of Pt nanoparticles. Additionally, metal oxides face limited electronic conductivity, adding to an additional barrier toward achieving high performance<sup>[30,31]</sup>.

Notably, several recent approaches have shown promising

results in achieving effective size control of Pt nanoparticles on highly graphitized carbon materials. For example, Zhi et al. reported a Pt catalyst supported by nitrogen-doped porous graphitic carbon that displayed high power density and exceptional carbon corrosion resistance<sup>[32]</sup>. The structurally doped nitrogen atoms in the support have the ability to interact with the Pt nanoparticles, which may favor better size control of the Pt nanoparticles. In addition, Watanabe's group demonstrated a nanocapsule method for synthesizing ~3 nm diameter Pt nanoparticles on graphitized carbon black<sup>[33,34]</sup>, which was developed based on a modification of the conventional colloid chemistry approach. Unfortunately, these innovative approaches involve either tedious or expensive synthetic processes, which hinders their practical use.

Herein, we report a scalable and simple method for the preparation of small Pt nanoparticles on graphitic carbons, which is based on a modification of the conventional impregnation-thermal reduction method that involves the use of mercaptopropane as the additive during the impregnation process. We demonstrate that mercaptopropane can coordinate with Pt during the impregnation process and subsequently convert into a sulfur-doped carbon shell coated on Pt nanoparticles during the following thermal reduction treatment. This can significantly suppress the migration and aggregation behavior of Pt nanoparticles on graphitic carbon, thereby achieving effective size control. Coupling this method with the optimization of the graphitization degree of the carbon support, we show a high-performance catalyst that fulfills the start-stop durability target set forth by the U.S. Department of Energy (DOE).

## 2 Experimental

### 2.1 Chemicals and reagents

Mercaptopropane (99.5%) was purchased from Aladdin (Shanghai, China). Hexachloroplatinic hexahydrate ( $\text{H}_2\text{PtCl}_6 \cdot 6\text{H}_2\text{O}$ , 99%), ethanol absolute (99.5%), and cyclohexane (99.8%) were obtained from Sinopharm Chemical Reagent Co. Ltd. (China). Deionized water (18.2 M $\Omega$ /cm) was used throughout the experiments. All chemicals were used as received without further purification.

### 2.2 Synthesis of graphitic carbons

Graphitic carbons with varying degrees of graphitization were prepared by subjecting carbon black (Ketjenblack EC-600J) to heat treatment at 2500 or 3000 °C for 1 h under argon (Ar) flow with a ramp rate of 500 °C/min.

### 2.3 Synthesis of graphitic carbon-supported Pt nanoparticles

The catalysts were prepared by the small molecule-assisted method that we recently developed for preparing intermetallic catalysts<sup>[35]</sup>. In a typical synthesis, 34 mg of  $\text{H}_2\text{PtCl}_6 \cdot 6\text{H}_2\text{O}$  (0.066 mmol) and 30  $\mu\text{L}$  of mercaptopropane (0.33 mmol) were first dissolved in 30 mL of cyclohexane by stirring in a 50 mL flask for 5 min. Next, 30 mg of graphitic carbon was added, and the mixture was stirred overnight to form a homogeneous dispersion solution. The resulting suspension was then dried using a rotary evaporator, followed by heat treatment at 300 °C for 2 h, and allowed to cool naturally to room

temperature to yield the final samples. The above synthetic protocols were also employed to prepare the contrast catalysts but without the addition of mercaptopropane.

### 2.4 Characterization

The X-ray diffraction (XRD) patterns were obtained by a Japan Rigaku DMax- $\gamma$ A rotating anode X-ray diffractometer with Cu K- $\alpha$  radiation. Ultraviolet–visible (UV–vis) absorption spectra were obtained on a UV-3600i plus spectrometer. Low-magnification high-angle annular dark-field scanning transmission electron microscopy (HAADF-STEM) images and energy-dispersive X-ray spectroscopy (EDS) mapping images were obtained by an FEI Talos F200X equipped with a Super X-EDS system. X-ray photoelectron spectroscopy (XPS) measurements were carried out on an ESCALab MKII X-ray photoelectron spectrometer. High-resolution bright-field STEM images were obtained by a JEM-ARM 200F atomic resolution analytical microscope. High-resolution transmission electron microscopy (TEM) images were obtained by an FEI Talos F200X. Inductively coupled plasma atomic emission spectrometry (ICP–AES) measurements were conducted by a Thermo Scientific iCAP 7400. X-ray absorption spectra were collected in the beamline 1W1B station of the Beijing Synchrotron Radiation Facility (BSRF).  $\text{N}_2$  adsorption/desorption isotherms were measured by ASAP 2020 (Micromeritics). Scanning electron microscopy (SEM) images were collected with a Zeiss Supra 40 scanning electron microscope.

### 2.5 PEMFC tests

**Membrane electrode assembly.** Catalyst-coated membranes (CCMs) were fabricated with an anode loading of 0.05 mg Pt per  $\text{cm}^2$  (TKK-30 wt% Pt/C) and a cathode loading of 0.1 mg Pt per  $\text{cm}^2$  (the prepared catalysts) with an ionomer (D2020® perfluorosulfonic acid ionomer) to carbon ratio (I : C ratio) of 0.6. The GORE Nafion membrane with a thickness of 8  $\mu\text{m}$  was used for the fabrication of CCMs. The membrane electrode assembly (MEA) was assembled by sandwiching the CCM between two 5  $\text{cm}^2$  gas diffusion layers (GDLs, Freudenberg H24CX483) with a thickness of 230  $\mu\text{m}$ . The gasket was a polytetrafluoroethylene (PTFE) film with a chosen thickness (140  $\mu\text{m}$ ).

**MEA testing protocols.** The MEAs were tested using a 7-channel serpentine flow field. Differential cell tests (5  $\text{cm}^2$ ) were conducted by the Scribner 850e fuel cell test stand linked with a Scribner 885 potentiostat.

**Voltage recovery.** The voltage recovery (VR) was conducted by scanning the voltage from the open circuit voltage to 0.1 V. Then, the cell potential was maintained at 0.1 V for 2 h at a temperature of 40 °C and a relative humidity (RH) of 150%, while being subjected to an absolute pressure of 150 kPa. During this period, the anode  $\text{H}_2$  flow rate was 500 sccm, and the cathode air flow rate was 2000 sccm. VR operation can greatly promote the performance of the cell, which has been previously demonstrated<sup>[36]</sup>.

**Polarization curves.** The  $\text{H}_2$ -air single-cell tests were operated at 80 °C/100% RH/150 kPa (absolute pressure).  $\text{H}_2$ /air flow rates were fixed at 500 and 2000 sccm, respectively. The cell voltage value was recorded at each current density for 3

min in the anodic direction.

**ECSA.** The Pt ECSA was determined using the hydrogen underpotential deposition (HUPD) method. During the measurement, the cell temperature was maintained at 40 °C, 100% RH and 100 kPa (absolute pressure). The cathode was purged with N<sub>2</sub> at a gas flow rate of 200 sccm until the voltage was swept from the open circuit voltage to less than 0.1 V. Subsequently, cyclic voltammetry (CV) was performed at a potential range from 0.03 V to 0.6 V, with a scan rate of 150 mV/s in an H<sub>2</sub> (200 sccm)/N<sub>2</sub> (5 sccm) environment. The ECSA was calculated according to  $ECSA = (S_{HUPD}/V)/(0.21 \times L_{Pt})$ , where  $S_{HUPD}$ ,  $V$ , and  $L_{Pt}$  represent the average integration area of both hydrogen adsorption and desorption peaks in the sweep speed, voltammogram, and Pt loading, respectively.

**Accelerated stress test (AST).** The catalyst support durability was tested by the AST protocol recommended by the U.S. DOE<sup>[9]</sup>. The fuel cell MEAs were cycled between 1 V and 1.5 V, with a triangle wave and a ramping rate of 500 mV/s. During the AST cycles, the cell was operated at 150 kPa (absolute pressure) H<sub>2</sub>/N<sub>2</sub>, 80 °C, 100% RH, with 200/75 sccm H<sub>2</sub>/N<sub>2</sub> for the anode and cathode, respectively.

### 3 Results and discussion

#### 3.1 Synthesis and characterization of graphitic carbons

We first employed the commercial carbon black Ketjenblack EC-600J (marked as KJ600) as the starting material to obtain graphitic carbon supports by high-temperature treatments. To investigate the impact of graphitization degree on the durability of carbon supports, we transformed KJ600 into graphitic carbons at two different temperatures (2500 °C and 3000 °C), which were denoted as KJ600-X, with X representing the processing temperature.

The XRD patterns of all resulting carbons are illustrated in Fig. 1a–c, wherein KJ600-2500 and KJ600-3000 exhibited a prominent diffraction peak at approximately 26.3°, corresponding to the (002) planes of the carbon material. The inter-layer spacing of the (002) plane of KJ600, KJ600-2500, and KJ600-3000 was determined to be 3.69, 3.45, and 3.38 Å, respectively. Moreover, with increasing processing temperature of KJ600, the (002) peak also exhibited a progressively narrower full width at half maximum (FWHM), with KJ600 (4.20) > KJ600-2500 (2.34) > KJ600-3000 (1.87). These results indicated an elevated degree of graphitization as the temperature increased<sup>[97]</sup>. To further elucidate the variances in graphitization degrees, Raman spectroscopy analyses were performed. As illustrated in Fig. 1d, all samples exhibited two distinctive peaks at 1350 cm<sup>-1</sup> and 1590 cm<sup>-1</sup>, representing the defect peak (D) and graphite lattice vibration peak (G) of the carbonaceous materials, respectively. The degree of graphitization can be quantified by the relative intensities of the D to G peaks, represented as  $I(D)/I(G)$ , where a smaller value of  $I(D)/I(G)$  indicates a higher degree of graphitization<sup>[98]</sup>. As shown by the calculated results, the  $I(D)/I(G)$  values decreased with an increase in temperature, with pristine KJ600 exhibiting the highest value (1.23), followed by KJ600-2500 (0.72) and KJ600-3000 (0.49). The nitrogen adsorption-desorption isotherms (Fig. 1e) showed a significant reduction in nitrogen uptake for high-temperature treated carbon materials over the entire relative pressure range compared to the original KJ600, indicating a decrease in porosity. The calculated specific surface area based on the Brunauer–Emmett–Teller (BET) equation and the pore volume calculated at a relative pressure of 0.99 both exhibited a decreasing trend with increasing temperature (Fig. 1f): KJ600 (1326 m<sup>2</sup>·g<sup>-1</sup> and 4.28 cm<sup>3</sup>·g<sup>-1</sup>) > KJ600-2500 (206 m<sup>2</sup>·g<sup>-1</sup> and 0.71 cm<sup>3</sup>·g<sup>-1</sup>) > KJ600-

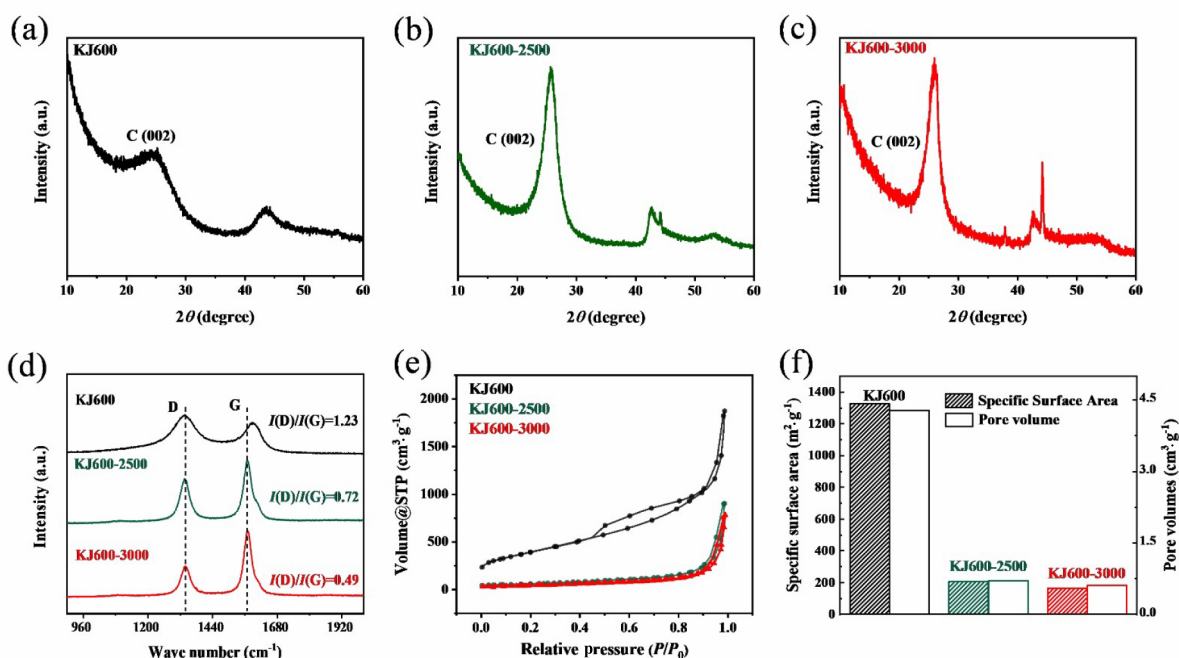


**Fig. 1.** (a–c) XRD patterns, (d) Raman spectra, (e) nitrogen adsorption-desorption isotherms, and (f) specific surface areas and pore volumes of KJ600, KJ600-2500, and KJ600-3000.



3000 ( $164 \text{ m}^2 \cdot \text{g}^{-1}$  and  $0.61 \text{ cm}^3 \cdot \text{g}^{-1}$ ).

### 3.2 Synthesis and characterization of graphitic carbon-supported Pt nanoparticles

We utilized the aforementioned graphitic carbon supports to fabricate Pt nanoparticle catalysts via the mercaptopropane-assisted impregnation-thermal reduction approach. First, the mercaptopropane additive and Pt salt precursor ( $\text{H}_2\text{PtCl}_6$ ) were impregnated onto graphitic carbon supports to achieve a total Pt loading of 30 wt%. The resulting powder precursors were then subjected to annealing treatments in 5 vol%  $\text{H}_2/\text{Ar}$  at  $300 \text{ }^\circ\text{C}$  for 2 h to obtain the Pt nanoparticle catalysts, which were marked as Pt-S/KJ600-X (X represents the processing temperature for the carbon supports). For comparison, we also prepared the Pt nanoparticle catalyst on the KJ600-3000 support without the use of mercaptopropane (denoted as Pt/KJ600-3000).

We analyzed the dispersion of the Pt nanoparticles on the carbon support by XRD patterns and TEM images. XRD patterns provided evidence for the positive effect of using mercaptopropane in achieving better size control of Pt nanoparticles, as supported by the fact that the half-peak breadth of Pt-S/KJ600-3000 at  $\sim 40.0^\circ$  was greater than that of Pt/KJ600-3000 (Fig. 2b and 2c). TEM images (Fig. 2d and 2e) demonstrated that mercaptopropane, when used as an additive, prevented the aggregation and overgrowth of Pt nano-

particles. Conversely, the Pt/KJ600-3000 catalyst exhibited an apparent increase in particle size and a heterogeneous distribution of Pt nanoparticles (Fig. 2f). The statistical results of TEM images (Fig. 2g–i) determined the average particle sizes of Pt-S/KJ600-2500, Pt-S/KJ600-3000, and Pt/KJ600-3000 to be 3.38, 3.80, and 7.00 nm, respectively.

### 3.3 Mechanism study

We employed the Pt-S/KJ600-3000 catalyst as an example to investigate how mercaptopropane is able to prevent the overgrowth of Pt nanoparticles on graphitic carbons. To do this, we conducted a comprehensive analysis of the structural changes of the Pt species during the entire catalyst preparation process using a range of characterization techniques, including UV–vis absorption spectroscopy, XPS, EXAFS, HAADF-STEM, high-resolution TEM, and EDS mapping.

The UV–vis spectra of  $\text{H}_2\text{PtCl}_6$  in ethanol/cyclohexane (Fig. 3a) showed characteristic absorption bands centered at 373 nm and 450 nm, which were attributed to *d-d* transitions of the octahedral symmetry of the  $[\text{PtCl}_6]^{2-}$  configuration<sup>[39,40]</sup>. Upon the addition of mercaptopropane to  $\text{H}_2\text{PtCl}_6$ , it was observed that the absorption band intensity significantly changed, indicating that the Cl ligands of  $[\text{PtCl}_6]^{2-}$  were substituted by sulfhydryl groups through ligand exchange<sup>[41]</sup>. The high-resolution Pt 4f XPS spectrum of  $\text{H}_2\text{PtCl}_6/\text{KJ600-3000}$  is shown in Fig. 3b. The peaks at 75/78 eV and 72.8/76.3 eV

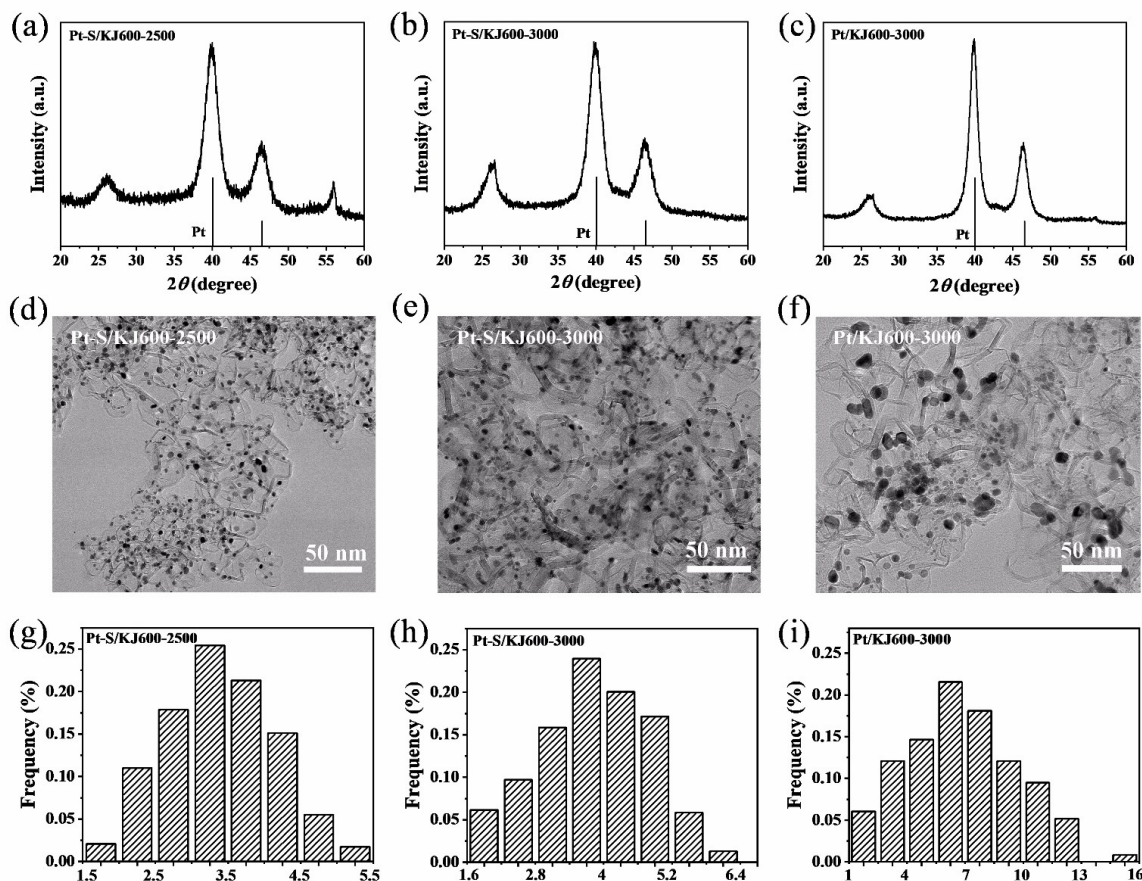


**Fig. 2.** (a–c) XRD patterns, (d–f) high-resolution TEM images, and (g–i) particle size distributions of Pt-S/KJ600-2500, Pt-S/KJ600-3000, and Pt/KJ600-3000. The particle size distributions were determined by the statistical results from high-resolution TEM images.

were assigned to Pt(IV) and Pt(II), respectively, indicating the presence of two oxidation states<sup>[42]</sup>. With the addition of mercaptopropene, the content of Pt(II) species increased, and the binding energy for Pt(IV) species negatively shifted, suggesting a more electron-enriched state due to ligand exchange. The Fourier transform EXAFS spectrum (Fig. 3c) showed an additional peak at 1.68 Å, which is similar to the Pt–S bond of PtS<sub>2</sub>, indicating a binding interaction between S and Pt atoms. These results suggest that the addition of mercaptopropene led to the formation of Pt–S bonds during the initial impregnation process.

High-resolution TEM imaging (Fig. 3d) revealed that, following thermal H<sub>2</sub> reduction, the as-formed Pt nanoparticles were coated by a thin carbon shell that was fused with the underlying graphitized carbon support. EDS elemental mapping images revealed a substantial concentration of S elements around the Pt particles (Fig. 3e). By taking into account the spatial relationship between the Pt particles, S, and carbon shells, it can be inferred that the S elements were doped into the carbon layers situated on the surface of the Pt nanoparticles. We previously found that the structurally doped S atoms in the carbon matrix can strongly interact with Pt nanoparticles to restrain their sintering under high temperature conditions<sup>[43]</sup>.

Based on the above results, we proposed a mechanism by which mercaptopropene achieves size control of Pt nanoparticles on graphitic carbons. The sulfhydryl group of mer-

captropene coordinates with Pt(IV) during the wet impregnation process, forming a coordination complex by partially exchanging with a Cl ligand. Upon thermal annealing, the complex precursors decompose to form Pt nanoparticles, while coordinated mercaptopropene ligands are converted into an S-doped carbon shell around the Pt nanoparticles. The physical protection of the carbon coating and the chemical Pt–S interaction work synergistically to greatly suppress Pt sintering during the thermal reduction process, ensuring the synthesis of small-sized Pt catalysts.

### 3.4 PEMFC performance and carbon support durability

We evaluated the PEMFC performance of the resulting catalysts in H<sub>2</sub>-air single cells at 80 °C, 100% RH and 150 kPa (absolute pressure) with a cathode loading of 0.1 mg·cm<sup>-2</sup>. Fig. 4a shows that within the practical operating voltage range of PEMFCs (0.6 to 0.7 V), the initial current density of the resulting catalysts followed the order of Pt-S/KJ600-2500 > Pt-S/KJ600-3000 > Pt/KJ600-3000. We attributed the higher current density of Pt-S/KJ600-3000 compared to that of Pt/KJ600-3000 to its smaller particle size, which can greatly improve the utilization rate of Pt atoms. Factoring in Pt-S/KJ600-2500 and Pt-S/KJ600-3000 have similar average particle sizes, and their differences in PEMFC performance may be due to varying degrees of graphitization, which may influence the interaction of the ionomer with the catalyst and consequently affect the performance.

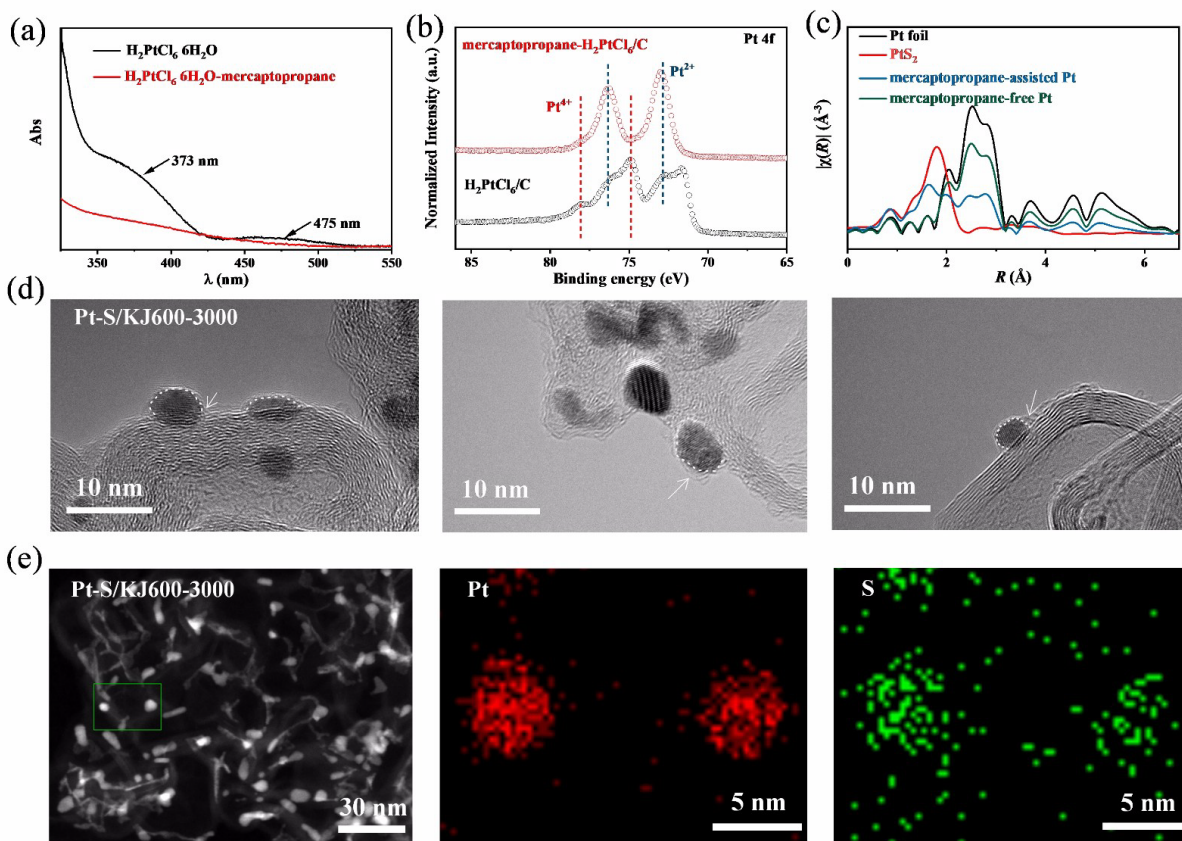


**Fig. 3.** (a) UV–vis spectra of the H<sub>2</sub>PtCl<sub>6</sub>·6H<sub>2</sub>O and H<sub>2</sub>PtCl<sub>6</sub>·6H<sub>2</sub>O/mercaptopropene solutions. (b) XPS results of the Pt 4f orbital of the mercaptopropene-Pt/C and Pt/C precursor powders. (c) R space of the XAFS results of the standard Pt foil, PtS<sub>2</sub>, and Pt catalysts prepared with and without mercaptopropene. (d) High-resolution TEM images of Pt-S/KJ600-3000. (e) HAADF-STEM and EDS mapping images of Pt-S/KJ600-3000.



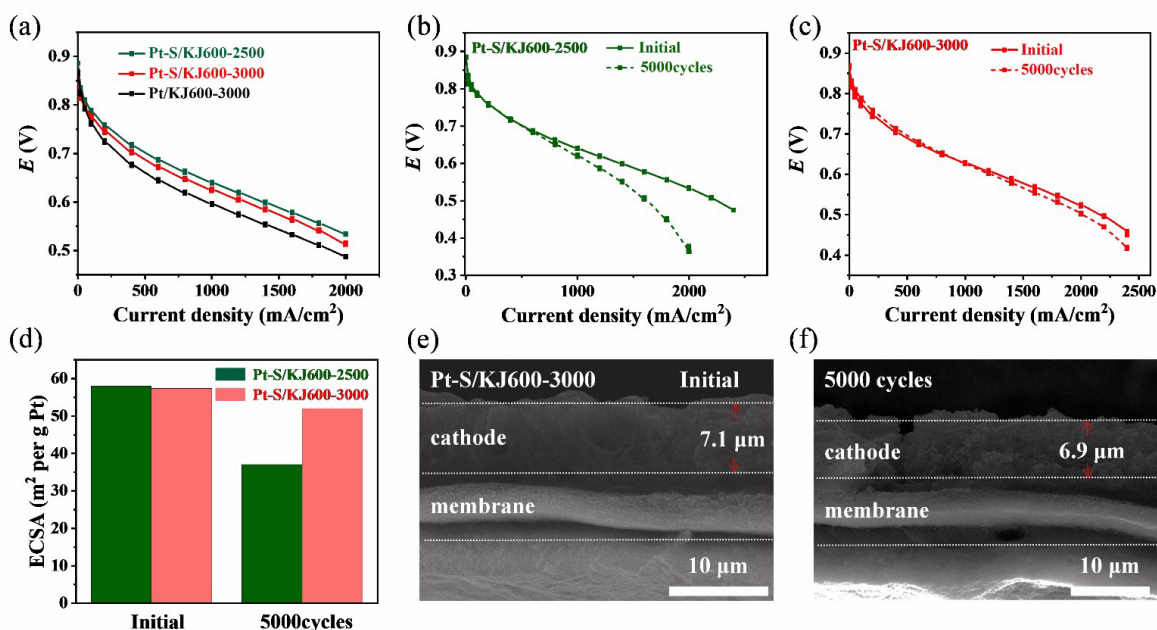


**Fig. 4.** (a) H<sub>2</sub>-air polarization curves of Pt-S/KJ600-2500, Pt-S/KJ600-3000 and Pt/KJ600-3000. (b, c) Durability of Pt-S/KJ600-2500 (b) and Pt-S/KJ600-3000 (c) after 5000 voltage cycles in the range of 1.0–1.5 V. (d) ECSA changes of Pt-S/KJ600-2500 and Pt-S/KJ600-3000 before and after 5000 voltage cycles in the range of 1.0–1.5 V. (e, f) SEM images of Pt-S/KJ600-3000 (e) before and (f) after 5000 voltage cycles in the range of 1.0–1.5 V.

We employed the accelerated stress test protocol recommended by the United States Department of Energy (DOE) to evaluate the start-stop durability of Pt-S/KJ600-2500 and Pt-S/KJ600-3000, which involved subjecting the catalysts to 5000 voltage cycles ranging from 1.0 to 1.5 V under a H<sub>2</sub>/N<sub>2</sub> environment. As depicted in Fig. 4b, the catalysts prepared with the KJ600-2500 support experienced a significant degradation in performance after 5000 cycles, manifesting in a substantial voltage drop of 75 mV at a current density of 1.5 A·cm<sup>-2</sup>. In contrast, Pt-S/KJ600-3000 (Fig. 4c) exhibited outstanding durability, with only a minor 10 mV loss observed at a current density of 1.5 A·cm<sup>-2</sup> after 5000 cycles, surpassing the DOE target of ≤ 30 mV loss. This difference in durability was further corroborated by ECSA results measured under PEMFC conditions (Fig. 4d), which revealed a considerably lower ECSA loss for Pt-S/KJ600-3000 (8.6%) relative to Pt-S/KJ600-2500 (35.3%). SEM observations of the electrode cross-sections were conducted to ascertain the changes in the thickness of the cathode catalyst layer after 5000 voltage cycles ranging from 1.0 to 1.5 V. As shown in Fig. 4e and 4f, the cathode catalyst layer thickness showed a negligible decrease (0.2 μm) when using KJ600-3000 as the catalyst support. These results highlighted the pivotal role of the degree of graphitization in determining the corrosion resistance of the carbon support.

## 4 Conclusions

In conclusion, we developed a mercaptopropane-assisted impregnation method for preparing small Pt nanoparticles on graphitic carbons. We revealed that the crucial role of mercaptopropane comes from its ability to convert into a thin sulfur-doped carbon shell on Pt nanoparticles during thermal treatment, which can effectively inhibit metal sintering by the

sulfur anchoring effect and/or the physical protection of the carbon coating. Compared to the conventional impregnation method, the catalyst prepared by this method exhibited much smaller particle sizes and thus resulted in a significantly improved cathode performance under H<sub>2</sub>-air PEMFC testing. By combining this method with the enhancement of the graphitization degree of graphitic carbon, we successfully obtained a catalyst that meets the support durability standards specified by the U.S. DOE. We believe that this method paves the way for low-cost and scalable fabrication of highly active Pt cathode catalysts with enhanced carbon corrosion resistance.

## Acknowledgements

This work was supported by the National Natural Science Foundation of China (22221003, 22071225), the Joint Funds from Hefei National Synchrotron Radiation Laboratory (KY2060000175), and the Fundamental Research Funds for the Central Universities (WK2060190103).

## Conflict of interest

The authors declare that they have no conflict of interest.

## Biographies

**Qian-Qian Yang** is presently a graduate student at the University of Science and Technology of China. Her research interests focus on the carbon support durability of fuel cell Pt cathode catalysts and the fabrication of small-sized Pt nanoparticles on graphitic carbons.

**Lei Tong** received his Ph.D. degree from the University of Science and Technology of China (USTC) in 2020 under the supervision of Prof. Hai-Wei Liang. Currently, he is a postdoctoral researcher at USTC working with Prof. Hai-Wei Liang. His research mainly focuses on the fabrication and application of Pt-based cathode catalysts for fuel cell applications.

**Hai-Wei Liang** received his Ph.D. degree under the supervision of Prof. Shu-Hong Yu at the University of Science and Technology of China (USTC) in 2011. Following this, he spent three and a half years as a postdoctoral fellow at the Max Planck Institute of Polymer Research (Germany), working alongside Prof. Klaus Müllen and Prof. Xinliang Feng. In 2016, he returned to USTC as a Full Professor. His research focuses on engineering the thermal decomposition chemistry of small molecules to synthesize functional carbon materials, as well as developing high-performance carbon-supported Pt and Pt alloy catalysts for fuel cell applications.

## References

- [1] Gröger O, Gasteiger H A, Suchsland J P. Erratum: Review—Electromobility: Batteries or fuel cells? [*J. Electrochem. Soc.*, 162, A2605 (2015)]. *J. Electrochem. Soc.*, **2016**, 163 (7): X3.
- [2] Gasteiger H A, Panels J E, Yan S G. Dependence of PEM fuel cell performance on catalyst loading. *J. Power Sources*, **2004**, 127 (1/2): 162–171.
- [3] Harzer G S, Schwämmlein J N, Damjanović A M, et al. Cathode loading impact on voltage cycling induced PEMFC degradation: A voltage loss analysis. *J. Electrochem. Soc.*, **2018**, 165 (6): F3118–F3131.
- [4] Nesselberger M, Ashton S, Meier J C, et al. The particle size effect on the oxygen reduction reaction activity of Pt catalysts: Influence of electrolyte and relation to single crystal models. *J. Am. Chem. Soc.*, **2011**, 133 (43): 17428–17433.
- [5] Stamenkovic V, Markovic N M. Tailored high performance low-PGM alloy cathode catalysts. In: 2018 DOE Hydrogen and Fuel Cells Program Review. The U.S. Department of Energy, **2018**.
- [6] Sattler M L, Ross P N. The surface structure of Pt crystallites supported on carbon black. *Ultramicroscopy*, **1986**, 20 (1/2): 21–28.
- [7] Mayrhofer K J J, Blizanac B B, Arenz M, et al. The impact of geometric and surface electronic properties of Pt-catalysts on the particle size effect in electrocatalysis. *J. Phys. Chem. B*, **2005**, 109 (30): 14433–14440.
- [8] Perez-Alonso F J, McCarthy D N, Nierhoff A, et al. The effect of size on the oxygen electroreduction activity of mass-selected platinum nanoparticles. *Angew. Chem. Int. Ed.*, **2012**, 51 (19): 4641–4643.
- [9] Sheng W, Chen S, Vescovo E, et al. Size influence on the oxygen reduction reaction activity and instability of supported Pt nanoparticles. *J. Electrochem. Soc.*, **2011**, 159 (2): B96–B103.
- [10] Meier J C, Galeano C, Katsounaros I, et al. Design criteria for stable Pt/C fuel cell catalysts. *Beilstein J. Nanotechnol.*, **2014**, 5 (1): 44–67.
- [11] Yin P, Hu S, Qian K, et al. Quantification of critical particle distance for mitigating catalyst sintering. *Nat. Commun.*, **2021**, 12 (1): 4865.
- [12] Padgett E, Yarlagadda V, Holtz M E, et al. Mitigation of PEM fuel cell catalyst degradation with porous carbon supports. *J. Electrochem. Soc.*, **2019**, 166 (4): F198–F207.
- [13] Reiser C A, Bregoli L, Patterson T W, et al. A reverse-current decay mechanism for fuel cells. *Electrochem. Solid-State Lett.*, **2005**, 8 (6): A273.
- [14] Mittermeier T, Weiß A, Hasché F, et al. PEM fuel cell start-up/shutdown losses vs temperature for non-graphitized and graphitized cathode carbon supports. *J. Electrochem. Soc.*, **2017**, 164 (2): F127–F137.
- [15] Tang H, Qi Z, Ramani M, et al. PEM fuel cell cathode carbon corrosion due to the formation of air/fuel boundary at the anode. *J. Power Sources*, **2006**, 158 (2): 1306–1312.
- [16] Devilliers D, Mahé É. Cellules électrochimiques: aspects thermodynamiques et cinétiques. *L'Actualité Chimique*, **2003**, 1: 31–40.
- [17] Yamashita Y, Itami S, Takano J, et al. Durability of Pt catalysts supported on graphitized carbon-black during gas-exchange start-up operation similar to that used for fuel cell vehicles. *J. Electrochem. Soc.*, **2016**, 163 (7): F644–F650.
- [18] Kneer A, Jankovic J, Susac D, et al. Correlation of changes in electrochemical and structural parameters due to voltage cycling induced degradation in PEM fuel cells. *J. Electrochem. Soc.*, **2018**, 165 (6): F3241–F3250.
- [19] Macauley N, Papadias D D, Fairweather J, et al. Carbon corrosion in PEM fuel cells and the development of accelerated stress tests. *J. Electrochem. Soc.*, **2018**, 165 (6): F3148–F3160.
- [20] Takahashi T, Ikeda T, Murata K, et al. Accelerated durability testing of fuel cell stacks for commercial automotive applications: A case study. *J. Electrochem. Soc.*, **2022**, 169 (4): 044523.
- [21] Borup R L, Kusoglu A, Neyerlin K C, et al. Recent developments in catalyst-related PEM fuel cell durability. *Curr. Opin. Electroche.*, **2020**, 21: 192–200.
- [22] Yu Y, Li H, Wang H, et al. A review on performance degradation of proton exchange membrane fuel cells during startup and shutdown processes: Causes, consequences, and mitigation strategies. *J. Power Sources*, **2012**, 205: 10–23.
- [23] Linse N, Scherer G G, Wokaun A, et al. Quantitative analysis of carbon corrosion during fuel cell start-up and shut-down by anode purging. *J. Power Sources*, **2012**, 219: 240–248.
- [24] Wang G J, Yu Y, Liu H, et al. Progress on design and development of polymer electrolyte membrane fuel cell systems for vehicle applications: A review. *Fuel Process. Technol.*, **2018**, 179: 203–228.
- [25] Zhang T, Wang P Q, Chen H C, et al. A review of automotive proton exchange membrane fuel cell degradation under start-stop operating condition. *Appl. Energy*, **2018**, 223: 249–262.
- [26] Higgins D, Hoque M A, Seo M H, et al. Development and simulation of sulfur-doped graphene supported platinum with exemplary stability and activity towards oxygen reduction. *Adv. Funct. Mater.*, **2014**, 24 (27): 4325–4336.
- [27] Parrondo J, Han T, Niangar E, et al. Platinum supported on titanium-ruthenium oxide is a remarkably stable electrocatalyst for hydrogen fuel cell vehicles. *Proc. Natl. Acad. Sci. U. S. A.*, **2014**, 111 (1): 45–50.
- [28] Huang S Y, Ganesan P, Park S, et al. Development of a titanium dioxide-supported platinum catalyst with ultrahigh stability for polymer electrolyte membrane fuel cell applications. *J. Am. Chem. Soc.*, **2009**, 131 (39): 13898–13899.
- [29] Zhang W, Cao Z, Zhang J, et al. Enhanced durability of Pt-based electrocatalysts in high-temperature polymer electrolyte membrane fuel cells using a graphitic carbon nitride nanosheet support. *ACS Sustainable Chem. Eng.*, **2020**, 8 (24): 9195–9205.
- [30] Wang L, Yue S, Zhang Q, et al. Morphological and chemical tuning of high-energy-density metal oxides for lithium ion battery electrode applications. *ACS Energy Lett.*, **2017**, 2 (6): 1465–1478.
- [31] Xiong W, Yin H, Wu T, et al. Challenges and opportunities of transition metal oxides as electrocatalysts. *Chem. Eur. J.*, **2023**, 29 (5): e202202872.
- [32] Qiao Z, Hwang S, Li X, et al. 3D porous graphitic nanocarbon for enhancing the performance and durability of Pt catalysts: A balance between graphitization and hierarchical porosity. *Energy Environ. Sci.*, **2019**, 12 (9): 2830–2841.
- [33] Yano H, Akiyama T, Bele P, et al. Durability of Pt/graphitized carbon catalysts for the oxygen reduction reaction prepared by the nanocapsule method. *Phys. Chem. Chem. Phys.*, **2010**, 12 (15): 3806–3814.
- [34] Lee M, Uchida M, Okaya K, et al. Durability of Pt/graphitized carbon catalyst prepared by the nanocapsule method for the start/stop operating condition of polymer electrolyte fuel cells. *Electrochemistry*, **2011**, 79 (5): 381–387.
- [35] Song T W, Xu C, Sheng Z T, et al. Small molecule-assisted synthesis of carbon supported platinum intermetallic fuel cell catalysts. *Nat. Commun.*, **2022**, 13 (1): 6521.
- [36] Kabir S, Myers D J, Kariuki N, et al. Elucidating the dynamic nature of fuel cell electrodes as a function of conditioning: An ex situ



- material characterization and in situ electrochemical diagnostic study. *ACS Appl. Mater. Inter.*, **2019**, *11* (48): 45016–45030.
- [37] Andrews R, Jacques D, Qian D, et al. Purification and structural annealing of multiwalled carbon nanotubes at graphitization temperatures. *Carbon*, **2001**, *39* (11): 1681–1687.
- [38] Endo M, Nishimura K, Kim Y A, et al. Raman spectroscopic characterization of submicron vapor-grown carbon fibers and carbon nanofibers obtained by pyrolyzing hydrocarbons. *J. Mater. Res.*, **1999**, *14* (12): 4474–4477.
- [39] Shelimov B, Lambert J F, Che M, et al. Initial steps of the alumina-supported platinum catalyst preparation: A molecular study by <sup>195</sup>Pt NMR, UV–visible, EXAFS, and Raman spectroscopy. *J. Catal.*, **1999**, *185* (2): 462–478.
- [40] Jin Z S, Chen Z S, Li Q L, et al. On the conditions and mechanism of PtO<sub>2</sub> formation in the photoinduced conversion of H<sub>2</sub>PtCl<sub>6</sub>. *J. Photoch. Photobio. A*, **1994**, *81*: 177–182.
- [41] Gomez S, Erades L, Philippot K, et al. Platinum colloids stabilized by bifunctional ligands: self-organization and connection to gold. *Chem. Commun.*, **2001**: 1474–1475.
- [42] Hidai S, Kobayashi M, Niwa H, et al. Platinum oxidation responsible for degradation of platinum-cobalt alloy cathode catalysts for polymer electrolyte fuel cells. *J. Power Sources*, **2012**, *215*: 233–239.
- [43] Yang C L, Wang L N, Yin P, et al. Sulfur-anchoring synthesis of platinum intermetallic nanoparticle catalysts for fuel cells. *Science*, **2021**, *374* (6566): 459–464.